

Deformation-Induced Planar Defects in *Immm* Ni₂(Cr, Mo, W) Strengthened HAYNES[®] 244[®] Superalloy



T.R. MANN, M.G. FAHRMANN, and M.S. TITUS

Precipitate shearing mechanisms during quasi-static elevated temperature tensile deformation and high temperature creep of *Immm* Ni₂(Cr, Mo, W) strengthened HAYNES[®] 244[®] alloy have been investigated. Interrupted tensile tests from room temperature to 760 °C (1400 °F) and creep tests at 138 to 693 MPa (20 to 100 ksi) and 649 °C to 760 °C (1200 °F to 1400 °F) were conducted to experimentally determine the active deformation mechanisms under relevant operating conditions. Stacking faults were observed to form in precipitates at the start of deformation by transmission electron microscopy diffraction contrast analysis. During subsequent deformation in these conditions, these stacking faults thickened into deformation microtwins at higher strains to accommodate plastic strain, which is contrary to many other Ni-based alloy systems where superlattice intrinsic and extrinsic stacking faults or coupled antiphase boundary shearing take place. This microtwinning deformation offers unique advantages to ductility and prevents debits in yield strength due to over aging. Microtwinning was observed across all strain rates, stresses, and temperatures investigated. The relative fault energies for the formation of these planar defects are discussed and compared to Density Functional Theory calculations.

<https://doi.org/10.1007/s11661-022-06945-2>

© The Minerals, Metals & Materials Society and ASM International 2023

I. INTRODUCTION

GAS turbine engines rely on advanced materials that can operate at elevated temperatures and in corrosive environments,^[1] and the operation of these engines at higher temperature improves performance and efficiency.^[2] The premier class of materials currently used in the hottest sections of the engine are Ni-base superalloys^[3] as these alloys provide an excellent combination of high temperature strength, creep resistance, oxidation resistance and fatigue life.^[1,4,5] Ni-based superalloys achieve high strength through the dispersion of coherent intermetallic phases within a solid-solution γ face-centered cubic matrix that resist dislocation motion. Most commercial alloys use γ' -(Ni₃Al) or γ'' -(Ni₃Nb) precipitates or a combination thereof to provide the high temperature strength,^[6-9] and the lower symmetry of the intermetallic phases causes the motion

of γ matrix dislocations through these precipitates to form planar defects such as an Antiphase Boundaries (APBs). These APBs are energetically unfavorable and require large stresses to form in the precipitate, thus strengthening the alloy.^[10-13]

The energetic pathway of dislocation motion has been investigated for several alloy systems, and the mechanisms determined from these calculations are complex and range from APB shearing to Superlattice Intrinsic/Extrinsic Stacking Fault formation (SISF/SESF) to microtwinning.^[14-23] The myriad of deformation modes arises largely from differences in symmetry and orientation relationships between the matrix and precipitate phases as well as the energies associated with the various planar faults that can form. The γ' -(Ni₃Al) has a L1₂ structure with cubic symmetry and forms a complex stacking fault (CSF) with any $\frac{a}{6}$ [112] partial dislocation Burgers vector. This is a high energy planar fault that resists slip of this partial dislocation. Instead, the dominant mechanism in γ' precipitates is either coupled dislocation shearing of SISF/SESF or APB planar defect formation as seen in a multiscale study by León-Cázares *et al.*^[24]

The other common precipitate phase, γ'' -(Ni₃Nb), exhibits a D0₂₂ structure with tetragonal symmetry. Though it has similar planar faults as γ' -(Ni₃Al), the tetragonal symmetry causes a low energy intrinsic

T.R. MANN and M.S. TITUS are with the School of Materials Engineering, Purdue University, West Lafayette, IN 47907. Contact e-mail: mann104@purdue.edu M.G. FAHRMANN is with the Haynes International Inc., Kokomo, IN 46901.

Manuscript submitted September 30, 2022; accepted December 17, 2022.

Article published online January 9, 2023

stacking fault along one slip system of $\frac{a}{6}[112]$ seen in the Generalized Stacking Fault Energy surface from Reference 25. The γ''' - $(\text{Ni}_2(\text{Cr}, \text{Mo}, \text{W}))$ phase that is used to strengthen HAYNES[®] 244[®] has an even lower symmetry body centered orthorhombic (BCO) structure. This novel strengthening phase has several $\frac{a}{6}[112]$ directions that form the intrinsic stacking faults, but others form APB and CSF planar defects with very high energy^[26] which influences the dislocation behavior in the alloy.

Previous studies investigating HAYNES[®] 242[®], which is strengthened through a similar γ''' - $\text{Ni}_2(\text{Cr}, \text{Mo})$ precipitate, have shown deformation twinning to be the dominant deformation mechanism during mechanical testing.^[27,28] Additionally, other research conducted on Pt₂Mo type intermetallic phases that are also body centered orthorhombic, in Ni–Cr and Ni–Cr–Mo alloys, has shown deformation twinning to be a significant deformation mechanism.^[29,30] This previous research indicated that dislocation interactions with the precipitates nucleated both type I and type II twins using the nomenclature of Christian and Laughlin.^[31] Type I twins are so called “true” twins which preserve the ordering of the superlattices but have a reflection on the twin plane. Type II twins or “pseudo” twins have the crystallographic reflection of twins but a violation of nearest neighbor bonding of the ordered structure. Kumar *et al.*^[27,32] proposed that the formation of stacking faults due to these interactions from the passage of an $\frac{a}{6}[112]$ partial dislocation in the precipitate occurs during the onset of deformation, and the passage of dislocations on subsequent (111) planes leads to multilayer stacking faults in the precipitate that thicken into both type I and type II deformation twins. This research focused on quasistatic room temperature tensile testing of various aged states for the 242 alloy. The exact mechanism of the initial stacking fault formation has not been entirely elucidated, but the prevalence of the twinning deformation is well-documented.

As a result, the primary motivation behind this manuscript stems from the lack of understanding of the onset of deformation in the Ni–Cr–Mo–W alloy system such as HAYNES[®] 244[®]. The macroscopic mechanical properties and behavior of this alloy such as high temperature tensile strength and creep are well studied.^[33] This alloy system has not been rigorously investigated on the initiation of deformation, and the role of the precipitates is not well understood. This manuscript covers the room temperature and elevated temperature quasi-static tensile testing and high temperature creep behavior of the 244 alloy and how the precipitation of the γ''' - $\text{Ni}_2(\text{Cr}, \text{Mo}, \text{W})$ phase changes the deformation mechanisms.

II. EXPERIMENTAL PROCEDURE

Material for this analysis was taken from a mill scale heat product at Haynes International’s Kokomo, IN mill. The nominal composition of this heat is 63.5Ni–22.5Mo–8Cr–6W (wt pct) (72Ni–15.6Mo–10.2Cr–2.2W (at. pct)). This heat was

cast and re-melted into a slab ingot that was homogenized, hot rolled into an intermediate slab, and subsequently hot rolled to 12.7 mm (0.5 inch) thick plate product. The plate was mill (solution) annealed at 1121 °C (2050 °F), followed by a water quench. In this condition, the microstructure features fully recrystallized, equiaxed grains, has a grain size of ASTM no. 4, and is free of large precipitates. Transverse 12.7 mm × 12.7 mm × 101.6 mm blanks were cut from this plate to be tested in quasi-static tensile deformation and tensile and compression creep deformation. The blanks were aged according to the following prescribed Haynes two-step heat treatment: 760 °C (1400 °F)/16 hours/furnace cool to 649 °C (1200 °F)/32 hours/air cool.

The sample blanks were aged before machining to reduce the cracking that can occur from residual stresses when aging post machining. The tensile samples were turned on a lathe to ASTM standard E8 small-size proportional to standard round specimens. The samples were 25.40 mm (1 in) in length at the gage section and 6.35 mm (0.25 in) in diameter. The tensile samples were deformed according to the ASTM standard E8 at a rate of $2.5 \times 10^{-4} \text{ s}^{-1}$ to 1 and 2 pct plastic deformation, then interrupted to examine the deformed microstructure. Interrupting the tensile tests at low plastic strain allows observation of the mechanisms that are operative at the initiation of deformation, but as noted later no difference in deformation mechanism is seen between 1 and 2 pct strain. The tensile tests were conducted at room temperature as well as 649 °C, 704 °C, and 760 °C (1200 °F, 1300 °F, and 1400 °F) to investigate the high temperature deformation the alloy might experience in service. An additional room temperature test on a mill annealed (unaged) sample was also conducted to compare the effect of aging and precipitate formation on dislocation motion. The tensile tests were conducted with an Instron Model 5985 load frame with a 250 kN max load capacity. The strain was measured with a calibrated Instron model PSH8MS extensometer.

Cylindrical compression creep blanks were machined with dimensions of 3 mm diameter and 8 mm tall, while tensile creep specimens were machined with gage sections of 3 mm diameter and gage lengths of nominally 25.4 mm. The creep samples were tested under constant load at 649 °C, 704 °C, and 760 °C (1200 °F, 1300 °F, and 1400 °F) and, similar to the tensile specimens, deformed to 2 pct plastic strain before interruption and cooling under load. Full creep curves till fracture were collected at Haynes Intl. Research and Technology department, but these samples are not characterized with TEM since the high plastic strain would obfuscate effective characterization of the steady-state creep regime. The stress applied to the creep samples varied between 138 to 693 MPa (20 to 100 ksi), and tests were conducted on an ATS model 2330SR automatic loading creep frame. Deformation was measured at a rate of 5 samples per minute during primary creep, and 1 sample per minute in subsequent creep with a calibrated transducer that measured the displacement of the extensometer frame fastened to the ends of the gage section in tensile specimen or the platens in the

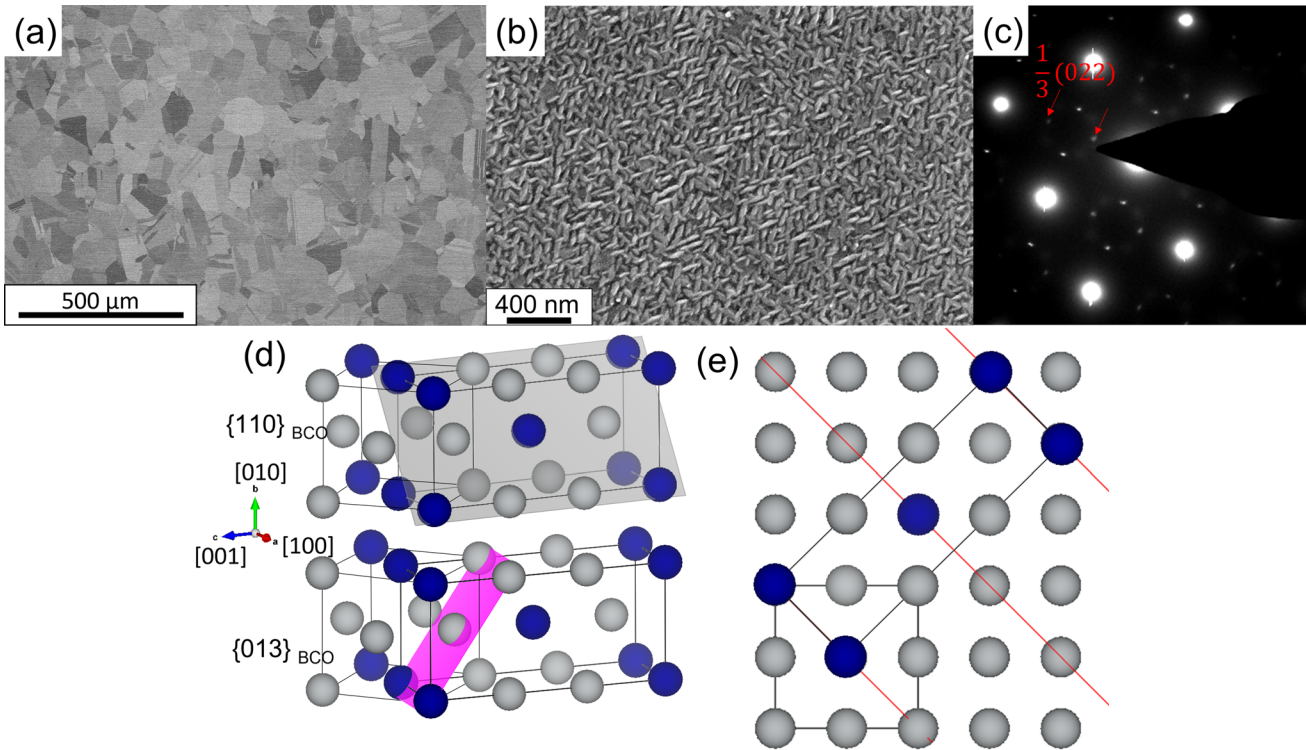


Fig. 1—(a) Backscatter Electron SEM micrograph in the polished and etched condition of the typical microstructure for the fully aged 244 alloy with annealing twins present in the alloy. (b) SEM in-lens image of the polished and etched microstructure of the fully aged condition. (c) TEM [001] SAED patterns of the microstructure showing the superlattice reflections of two variants of the $\text{Ni}_2(\text{Cr, Mo, W})$ precipitates after the full aging heat treatment. (d) The unit cell of the BCO structure showing the orientation relationship with the FCC matrix and the two distinct close packed planes. (e) A schematic showing every $1/3$ (220) plane corresponds with the BCO symmetry in the FCC lattice.

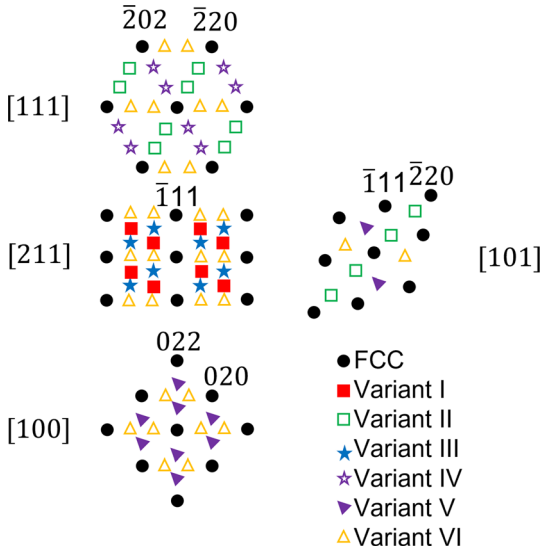


Fig. 2—A schematic illustration of all the possible variant superlattice reflections for the [111], [211], [101], and [100] zone axes. Reproduced from Song *et al.*^[36]

compression specimens. While compression creep samples will not exhibit rupture lives and tertiary creep similar to tensile creep samples, the minimum creep rate during secondary creep are expected to be similar. The

deformation mechanism was not seen to change between compression and tension. Tension and compression creep behavior asymmetry is seen in single crystal Ni-based superalloys such as CMSX-4 and TMS-75 due to different operative deformation mechanisms,^[34] but these were not seen in the polycrystalline HAYNES® 244®.

Deformed specimens were sectioned perpendicular to the loading axis. For general microstructure analysis, specimens were mechanically ground and polished using silicon carbide grinding paper and diamond suspension down to $1 \mu\text{m}$ diameter. Metallography samples were electroetched with a solution of 95 pct hydrochloric acid and 5 pct oxalic acid and 6 V DC voltage. A FEI Quanta 650 scanning electron microscope was operated at 20 keV in backscatter electron imaging mode to characterize the general microstructure. For deformation microstructures, transverse discs were sectioned from the gage section and mechanically polished using 320 and 800 grit silicon carbide polishing paper to a thickness of $100 \mu\text{m}$. Transmission electron microscopy samples were prepared using a twin-jet Tenupol-5 electropolisher operating at 30 V and 100 mA at -30°C in a 7.5 pct perchloric acid – 92.5 pct methanol (by volume) bath. TEM microstructure analysis was performed on Tecnai T20 TEM with 200 keV accelerating voltage and an FEI Talos F200X with 200 keV accelerating voltage. Both Bright Field and Dark field diffraction contrast imaging modes were used to

Table I. Orientation Relationships Between the FCC Matrix (M) and the γ''' Precipitate (p) Variants

Variant	Relationship
I	$[001]_p \parallel [110]_M; [010]_p \parallel [\bar{1}10]_M; [100]_p \parallel [001]_M$
II	$[001]_p \parallel [1\bar{1}0]_M; [010]_p \parallel [110]_M; [100]_p \parallel [001]_M$
III	$[001]_p \parallel [101]_M; [010]_p \parallel [10\bar{1}]_M; [100]_p \parallel [010]_M$
IV	$[001]_p \parallel [\bar{1}01]_M; [010]_p \parallel [101]_M; [100]_p \parallel [010]_M$
V	$[001]_p \parallel [011]_M; [010]_p \parallel [0\bar{1}1]_M; [100]_p \parallel [100]_M$
VI	$[001]_p \parallel [01\bar{1}]_M; [010]_p \parallel [011]_M; [100]_p \parallel [100]_M$

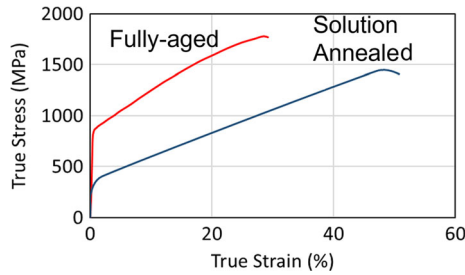


Fig. 3—The stress strain curve for the room temperature fully age hardened 244 alloy and the mill annealed (precipitate-free) sample. Although the alloy is fully aged, it shows significant ductility and work hardening for a high strength Ni-base superalloy. The annealed sample showed more ductility but drastically lower yield strength.

characterize the deformation in these samples. To image in bright field and the two-beam dark field diffraction condition, a dual axis tilt holder was used on both microscopes.

III. RESULTS

A. Microstructure

The aged microstructure exhibits an ASTM grain size of 4, small grain boundary carbides, annealing twins, and a fine distribution of the γ''' *Immm* Ni₂(Cr, Mo, W) precipitates, as shown in Figure 1. The precipitates form six different variants due to the orientation relationships with matrix^[33] and exhibit lenticular morphologies anisotropic (albeit rather small) lattice mismatch between matrix and the BCO phase resulting from the high concentration of the Mo in the alloy.^[35] The fully aged precipitate size is approximately 200 nm in length along the long axis and 80 nm in length along the shortest axis. The precipitate variants are equally distributed throughout the grains, and there are no precipitate-free zones. The morphology of the

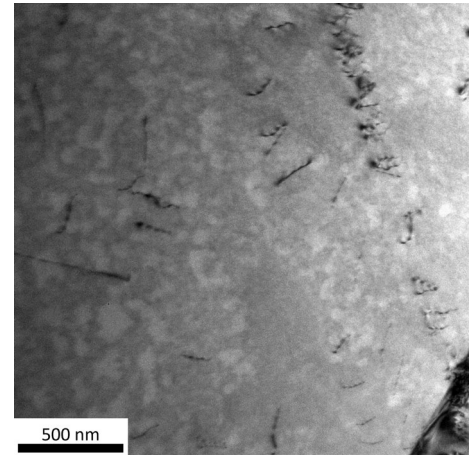


Fig. 4—Mill annealed (precipitate-free) specimen deformed under tension at $2.5 \times 10^{-4} \text{ s}^{-1}$ to 2 pct strain. The BF TEM image shows dislocations arranged in a planar slip configuration, approaching a grain boundary in the lower right.

precipitates indicates that all 6 variants are statistically represented in a grain. The alloy contains approximately 40 pct by volume of γ''' precipitates using image analysis of the etched SEM images; however, precise measurements are difficult to ascertain due to the morphology and orientation of the precipitates. During TEM characterization, all variant superlattice reflections in the various Selected Area Electron Diffraction (SAED) patterns were seen, as shown in Figure 1(c), indicating the presence of every variant on the different SAED patterns. These superlattice reflections occur at $1/3$ (022) planes highlighted in the figure and at $1/3$ (420) planes which corresponds with the *Immm* BCO symmetry. Simulations of the superlattice reflections for every variant can be found in a recent work by Song *et al.*^[36] and shown reproduced in Figure 2. Table I indicates the orientation relationships of the different variants with the FCC matrix.

B. Tensile Deformed Samples

In the mill annealed (precipitate-free) specimen, dislocations were observed, as shown in Figure 4. Many series of individual $\frac{a}{2}[110]$ matrix dislocations are observed in a planar configuration, indicating planar slip at room temperature. This specimen had a yield strength of 395 MPa and a total elongation of 66 pct as expected for a solution annealed sample shown in Figure 3.

In fully aged specimens, the 0.2 pct offset yield is approximately 836 MPa with an average total of 34 pct elongation at rupture in the aged condition seen in the stress strain curve of Figure 3. Deformation twinning was observed across all temperatures investigated in quasi-static tensile testing. From room temperature to 760 °C, microtwins that extend across the entire length of the grains were seen in the prepared TEM foils, as shown in Figures 5(a) and (b). Confirmation of the microtwins is shown in the SAED pattern along the $[110]$ zone axis, as shown in Figures 5(c) and (d). The

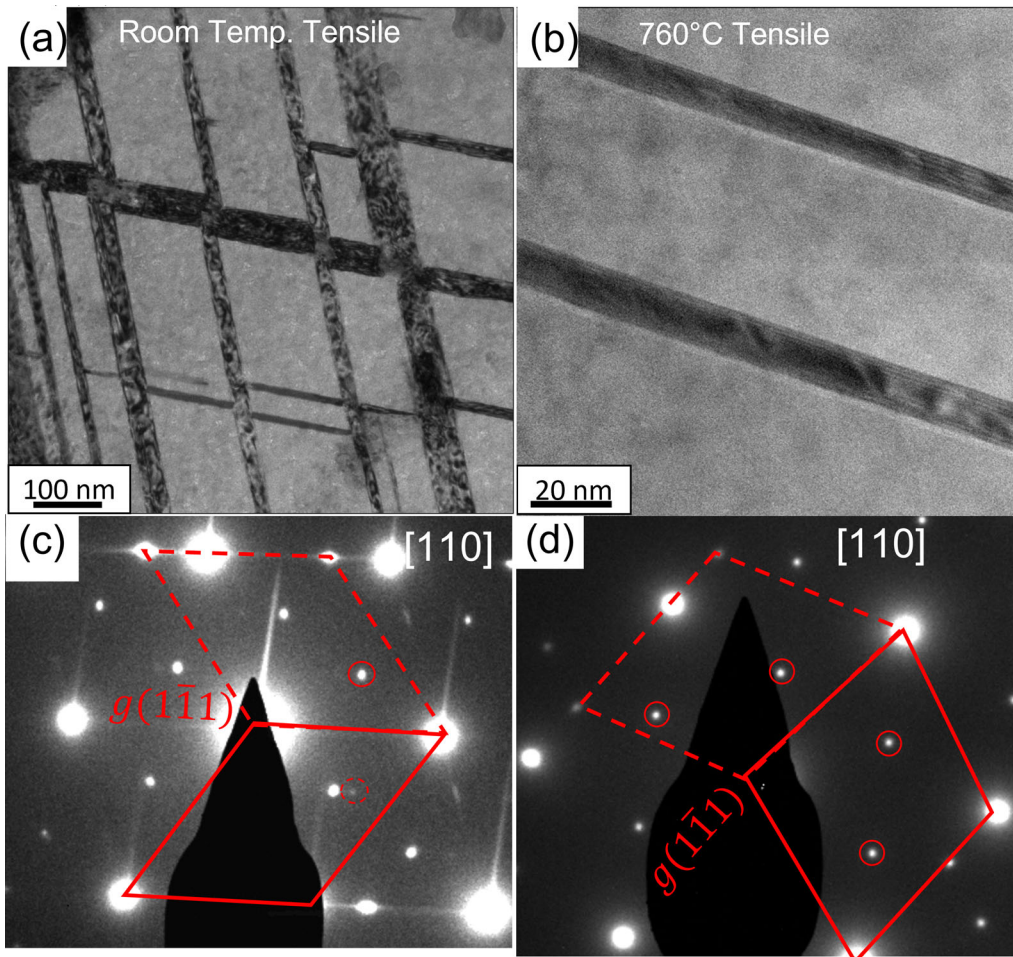


Fig. 5—(a) Bright field conventional TEM images of deformation microtwins in the room temperature deformed tensile sample interrupted at 2 pct. (b) Bright Field TEM images of deformation microtwins from 760 °C tensile deformation interrupted at 2 pct. Both images are taken off the zone axis shown in (c) and (d), using a small objective aperture to generate good contrast with the twinned regions. (c) and (d) [110] zone axis SAED patterns for (a) and (b), respectively. Clear matrix twin reflections are noted with a red, dashed parallelogram reflected about a $1\bar{1}1$ g vector. The precipitate presence is shown in the SAED superlattice reflections highlighted with red circles. The pattern in (c) also shows the superlattice reflection with a dashed red circle (Color figure online).

twins are shown as a mirror (or 180 deg rotation, an equivalent transformation) about the $\{111\}$ diffraction spots for the FCC lattice. Figure 5(a) shows two variants of twin formation with two similar Schmid factors which can also be seen in the SAED pattern in Figure 5(c). These twins formed through both the matrix and precipitates as shown in Figure 6.

Intrinsic and Extrinsic stacking faults were observed in tensile specimens deformed to 2 pct strain, as shown in Figure 7. Dark field imaging was used to determine the nature of the planar faults. The direction of the g vector indicates whether the fault is intrinsic or extrinsic in displaced aperture dark field imaging. Determining the intrinsic or extrinsic nature of the fault depends on whether the g vector points towards or away from bright fringes of the fault.^[37] The $g(1\bar{1}1)$ of the $[121]$ zone axis vector points towards the outermost bright fringe in the dark field image for ESF1 and ESF2, indicating that the faults are extrinsic, whereas the same g vector points away from the outermost bright fringe (faintly observed on the right side) for the defect labeled ISF, indicating

that the fault is intrinsic. This is confirmed using an atomic resolution conventional TEM image shown in Figure 7(c). Conventional TEM imaging of atomic resolution is not as reliable as STEM characterization of the faults although the faults can still be seen by the stacking sequence interruption showing intrinsic or extrinsic stacking. Figure 7(c) shows the faults are intersecting likely limiting the growth of these faults into microtwins.

C. Creep Deformed Samples

High temperature creep behavior generally exhibited limited primary creep strain followed by extended periods of steady-state creep, especially at lower temperatures. The influence of the applied stress and test temperature at 649 °C, 704 °C, and 760 °C on the creep behavior is shown in Figure 8. At 760 °C a 104 MPa increase in applied stress decreased the time to reach 2 pct plastic strain by a factor of 8.6, but at 649 °C, increasing the stress by 55 MPa decreased the time to 2

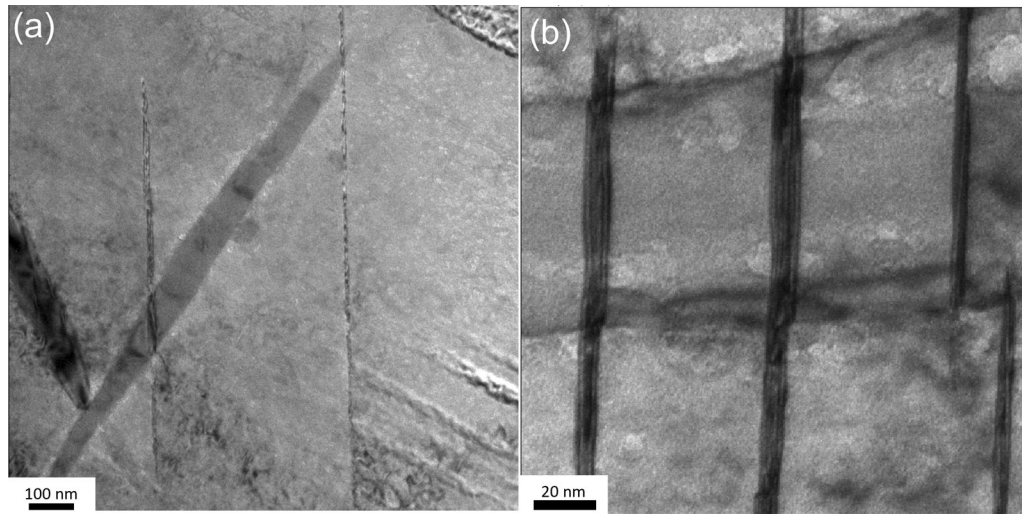


Fig. 6—Bright Field TEM images of thin deformation microtwins shearing through a γ''' precipitate in the 649 °C tensile deformed sample interrupted at 2 pct. These twins are characterized by the SAED patterns similar to Fig. 5 but imaged in 220 g vector two-beam condition off the [110] axis to show the precipitate contrast. The lower right side of (a) shows some twin variants that do not have significant contrast in bright field imaging with an aperture. (b) Shows a higher magnification image of the microtwins passing through the precipitate-matrix interface.

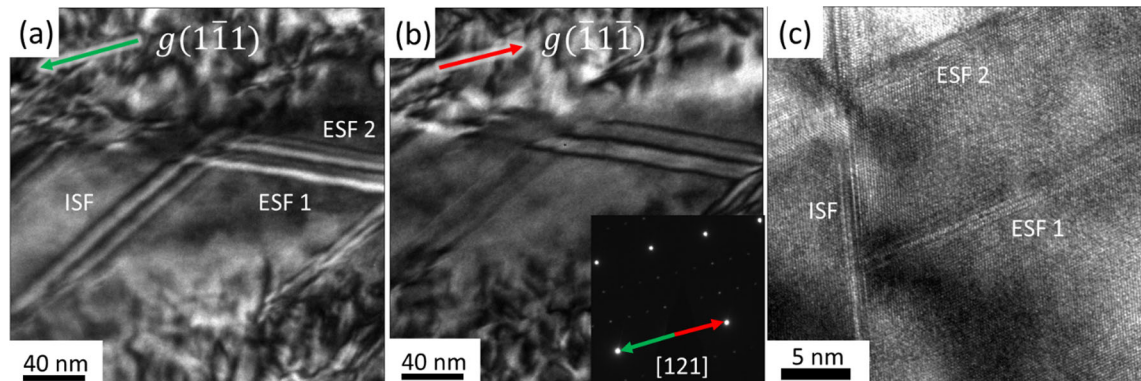


Fig. 7—(a) and (b) Displaced Aperture Dark Field Diffraction contrast TEM images of the formation of the intrinsic and extrinsic stacking faults in the precipitate. This sample was tensile deformed to 2 pct strain at room temperature. (c) Atomic resolution conventional TEM image on a [110] zone axis of the same faults showing the faults are intersecting.

pct plastic strain by a factor of 20.1. These stresses were chosen after reviewing several high temperature creep tests conducted at Haynes Intl. Research and Technology Department and selecting a stress that would produce suitable creep lifetimes.

The minimum steady-state creep rate was calculated from the creep strain curves to determine the creep behavior and follows a power law relationship with the applied stress. The minimum steady-state creep rate is shown in Figure 9 for the three temperatures investigated. The stress exponents for these tests were 9.6, 7.9, and 4.6 for the 649 °C, 704 °C, and 760 °C tests, respectively. The stress exponent increases at lower temperatures but fundamentally the mechanism that occurs in these tested samples does not change, and they still maintain creep exponents consistent with power law creep. Figure 9 shows the minimum creep rate for additional tests conducted at Haynes Intl. Research and Technology Department (filled, non-outlined data

points) as well as the compression tested samples tested using the methods outlined above (unfilled, outlined data points). All tests conducted at Purdue University using methods outlined above and reported with TEM results are outlined in black. The creep curves and strain rates of the Haynes tests are provided in the supplemental information.

Microtwinning was once again observed as the dominant deformation mechanism at strains as low as 2 pct and up to rupture across all temperatures and stresses in both the tension and compression creep testes samples. The 760 °C and 704 °C temperature tested samples did show a significant microstructural evolution of precipitate realignment in the twinned regions but still significant deformation twinning. An example of the extent of deformation twinning from the 649 °C, 414 MPa specimen tested to rupture (5.3 pct, 9532 hours) is shown in the secondary electron SEM image in Figure 10. All grains in this specimen showed

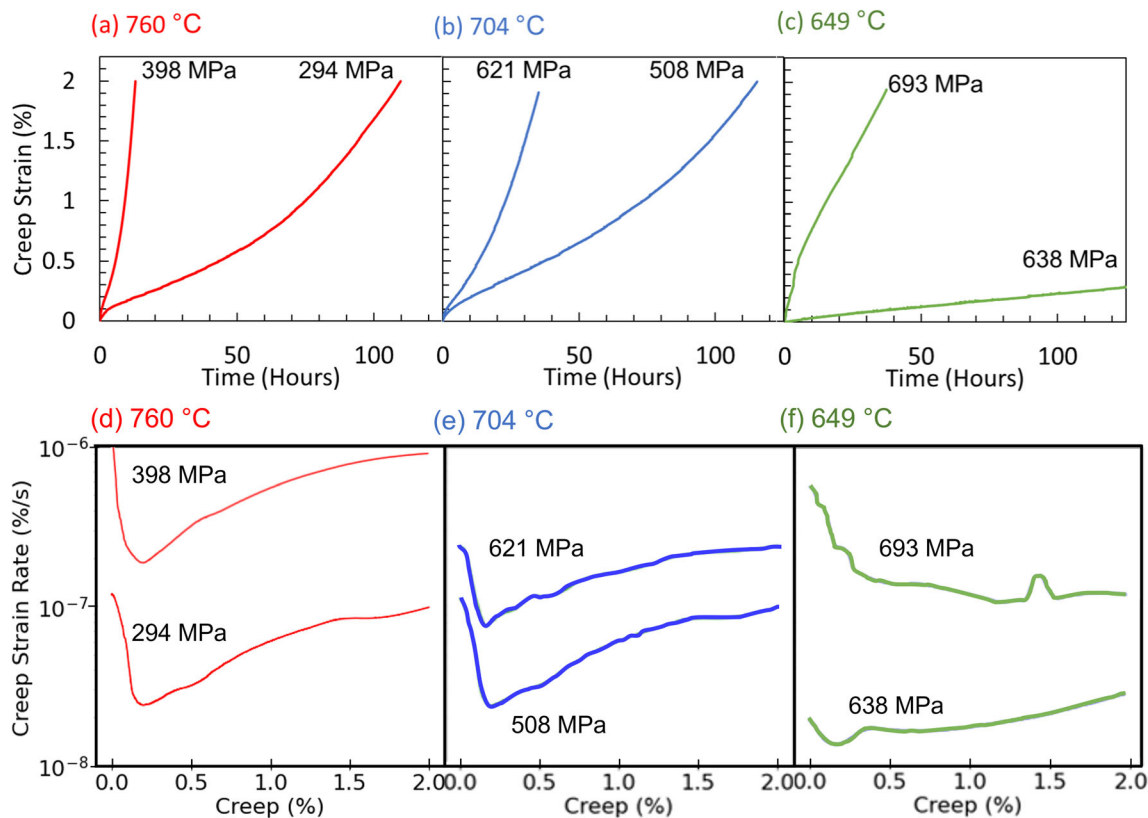


Fig. 8—(a) through (c) The interrupted creep curves for various temperatures and stresses. The 649 °C 638 MPa test extends to 700 h to reach the 2 pct interruption. (d) through (f) Calculated creep strain rates as a function of plastic strain. These curves show how the higher temperatures do not have an extended region of steady-state creep rate as opposed to the tests at 649 °C.

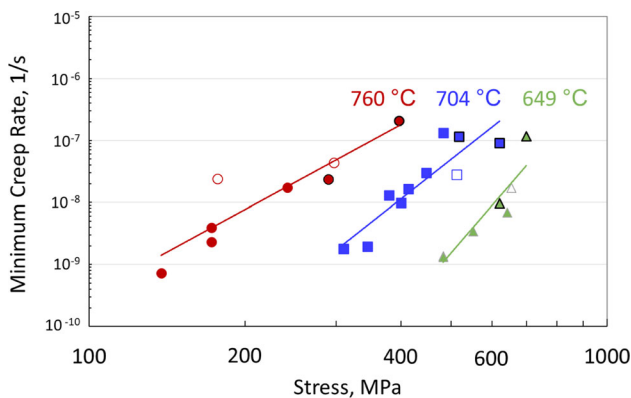


Fig. 9—The minimum creep rate as a function of applied stress for the creep tests conducted at various temperatures. The line shown here represents the stress exponent for a power law relationship. Filled shapes indicate tensile tested creep samples, unfilled is compression tested creep samples, and bordered and marked shapes are the tests referenced above.

evidence of microtwin formation, as evidenced by the surface steps resulting from the etched microstructure. At and below 2 pct creep strain, faint evidence of microtwins could be observed *via* SEM, but many microtwins could be observed in TEM foils, as shown in Figure 11. Here, microtwins are observed both in the precipitate and the matrix, similar to that observed from

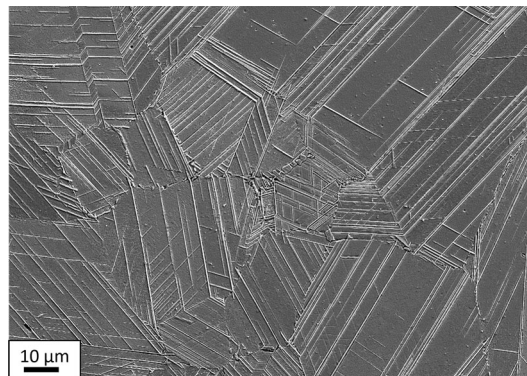


Fig. 10—A SEM secondary electron image in the etched condition of the 649 °C, 414 MPa creep specimen. The duration of this test was 9532 h, and the specimen ruptured at 5.3 pct strain.

tensile tests in Figure 6. The darkfield image in Figure 11 shows extended stacking faults alongside fully formed deformation twins.

The higher temperature creep tests (every 760 °C test and the 704 °C tests at stresses above 450 MPa) did not exhibit an extended steady-state creep regime and instead exhibited a relatively short transient minimum creep rate. At stresses below 400 MPa, the 704 °C creep tests showed longer regions of minimum creep rate, but still transient. This is likely due to microstructural

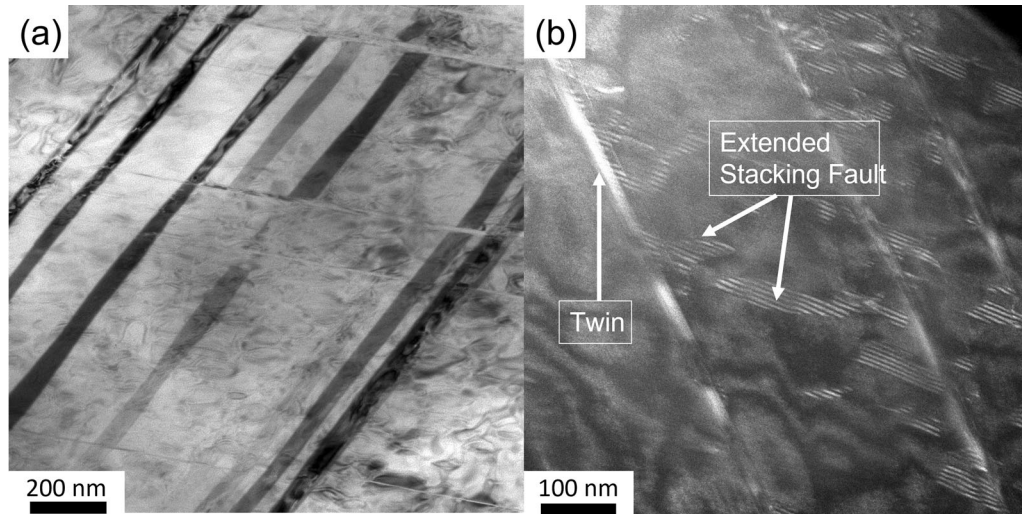


Fig. 11—Deformation twinning and extended stacking faults in 649 °C and 704 °C creep deformed samples. (a) is a bright field TEM image using an aperture to remove twin reflection intensities. Some deformation twin variants do not have good contrast indicating that they have different habit planes. (b) shows a displaced aperture dark field image of fully formed twins and extended stacking faults in the precipitates and matrix that formed during creep deformation.

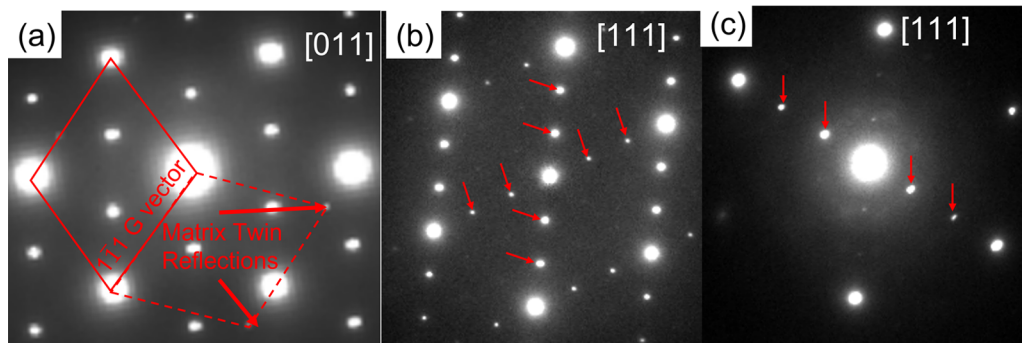


Fig. 12—(a) [110] Zone Axis SAED of the 760 °C creep sample tested at 294 MPa and interrupted at 2 pct, showing the twin reflections (red, dashed parallelogram). SAED images showing (b) the [111] Zone Axis in a non-twinned region with corresponding disappearance of the $1/3\{022\}$ superlattice reflections and (c) the same [111] Zone Axis in a twinned region with the reappearance of the superlattice reflections (red arrows) (Color figure online).

Table II. Summary of Tensile Data

Condition	Temperature (°C)	Strain Rate (10^{-4} s^{-1})	0.2 Pct Yield Stress (MPa)	Ultimate Tensile Strength (MPa)	Elongation (Pct)
Mill Annealed	27	2.5	395	900	66
Fully Aged	27	2.5	836	1345	34
Fully Aged	649	2.5	647	975	21
Fully Aged	704	2.5	585	866	18
Fully Aged	760	2.5	463	696	44

Table III. Summary of Creep Data for the TEM Investigated Tensile Creep Samples

Condition	Temperature (°C)	Stress (MPa)	Min. Creep Rate (s^{-1})	End of Test	Time to End (h)
Fully Aged	649	693	1.17×10^{-7}	2 pct (interrupted)	35.1
Fully Aged	649	638	1.69×10^{-8}	2 pct (interrupted)	704.7
Fully Aged	704	621	1.34×10^{-7}	2 pct (interrupted)	34.9
Fully Aged	704	508	2.80×10^{-8}	2 pct (interrupted)	114.5
Fully Aged	760	398	2.09×10^{-7}	2 pct (interrupted)	12.7
Fully Aged	760	294	2.33×10^{-8}	2 pct (interrupted)	109.1

evolution at this higher temperature, as evidenced by the disappearance of certain precipitate superlattice reflections in the non-twinned region, and appearance of the same reflections in the twinned region, as shown in Figure 12. These SAEDs show this microstructural evolution occurring in the regions that are twinning. The anisotropic coherency stress associated with the lenticular precipitates is likely facilitating this variant selection during creep testing.

All temperatures and stresses resulted in deformation twinning in the examined creep samples. Extended stacking faults were also observed in the microstructure next to fully formed deformation twins. Tables II and III show a summary of the tensile mechanical properties for the 244 alloy and the creep properties.

IV. DISCUSSION

Deformation twinning dominates the plastic deformation of the HAYNES® 244® alloy at temperatures and strain rates ranging from 27 °C to 760 °C and 10^{-4} to 10^{-9} s $^{-1}$, respectively. Based on prior work^[27,28,32] and our recent^[26] and current findings, we hypothesize that the formation of planar defects in the precipitates at the initiation of deformation is the origin of the deformation twinning. It is clear that the γ''' precipitates are responsible for the formation of these planar defects and eventual microtwins because these they are not observed in the mill annealed (precipitate-free) microstructure but are instead observed in all γ''' -containing specimens. Thus, the underlying mechanism for formation of the microtwin arises from the interplay of the six unique γ''' variants, and it is likely that each variant is required to be present for microtwin formation to take place.

Take, for example, a perfect $\frac{a}{2}110$ matrix dislocation gliding through the matrix and interacting with one of six precipitates (Figure 13(a)). Based on our prior work^[26] and the orientation relationships of the γ''' variants, one of three interactions will initially take place:

- The $\frac{a}{2}110$ will be blocked due to the formation of (i) a high energy CSF from the leading $\frac{a}{6}121$ partial dislocation and (ii) a subsequent high energy APB from the trailing $\frac{a}{6}21\bar{1}$ dislocation (Figure 13(b), red particle). This GSFE pathway has a multiplicity of two.
- The $\frac{a}{2}110$ will easily pass through because it is a perfect translation vector of the γ''' in this particular orientation (Figure 13(b), green particle). This GSFE pathway has a multiplicity of one.
- The $\frac{a}{2}110$ will dissociate with the leading partial forming an ISF, and the trailing being pinned at the interface due to the formation of a high energy APB (Figure 13(c), top). If subsequent $\frac{a}{2}110$ dislocations shear on adjacent planes, this ISF will thicken into an ESF and eventually a microtwin (Figure 13(c), middle and bottom). This GSFE pathway has a multiplicity of three.

To verify these energy pathways, we calculated the partial GSFE pathway using methodologies from Reference 26 of these three γ''' orientations (Figure 13(d)), including that of the ESF which would form by the passage of an $\frac{a}{2}110$ dislocation on an adjacent plane to an ISF (Figure 13(e)). While the ESF pathway and energy (210 mJ/m 2) is not as low energy as the ‘perfect crystal pathway’ with an ISF (140 mJ/m 2) denoted in Figure 13(d), it is still approximately half the energy of the APB (410 mJ/m 2). Compared to other modes of shearing, the ESF pathway is thus viable, especially considering three of the six variants will accommodate this shearing mode.

Extended stacking faults formed from the passage of two partial dislocations have been observed in other Ni-based superalloys at elevated temperature^[9,37] especially with large precipitates or complex planar defect pathways. Extrinsic stacking faults behave as a nucleus of a deformation twin as there is a reflection now along the unsheared plane shown in Figure 13(e). Once these extrinsic faults and microtwins begin to form, subsequent dislocations again move to the boundary and slip along the boundary ultimately thickening the deformation microtwin and accommodating the plastic strain.

To illustrate how a field of precipitates might interact with an $\frac{a}{2}110$ dislocation, a representative schematic is shown in Figure 14 with a ratio of 1:2:3 for the green, red, and orange precipitates, respectively, which represent each of the six possible variants. When the matrix dislocation interacts with the red (CSF-forming) precipitate, passing is only possible through Orowan looping, as shown in the upper left of Figure 14. Meanwhile, green precipitates (where an $\frac{a}{2}110$ dislocation will fully translate the γ''' lattice) will not act as a significant barrier to dislocation motion. Finally, the orange precipitates (ISF-forming) will initially allow for extended ISFs to form upon passage of the leading partial dislocation, and at higher stresses, the trailing partial will eventually loop around the precipitate. In between passage of the leading, ISF-forming partial, and subsequent looping of the trailing partial dislocation, the leading partial may significantly dissociate and even escape the trailing if the precipitate field ahead is made up of other orange or green precipitates. This could be why we observe semi-isolated and extended faults in deformed specimens, as shown in Figure 11.

Eventually subsequent $\frac{a}{2}110$ matrix dislocations on adjacent planes will interact with these extended ISFs to form ESFs and microtwins. Upon their formation, their cooperative motion likely significantly lowers the energy barrier for shearing, and cascades of dislocations dissociate from their trailing partial dislocations. Thus, the strength of this material may be controlled by either the spacing of the red (CSF-forming precipitates), akin to an Orowan bowing mechanism, or by the requirement of dislocations to cooperatively shear through precipitates in a microtwin formation.

The result of this low energy ESF to microtwin pathway of deformation allows the alloy to exhibit significant ductility at room temperature as well as at higher temperatures. This twinning mechanism also

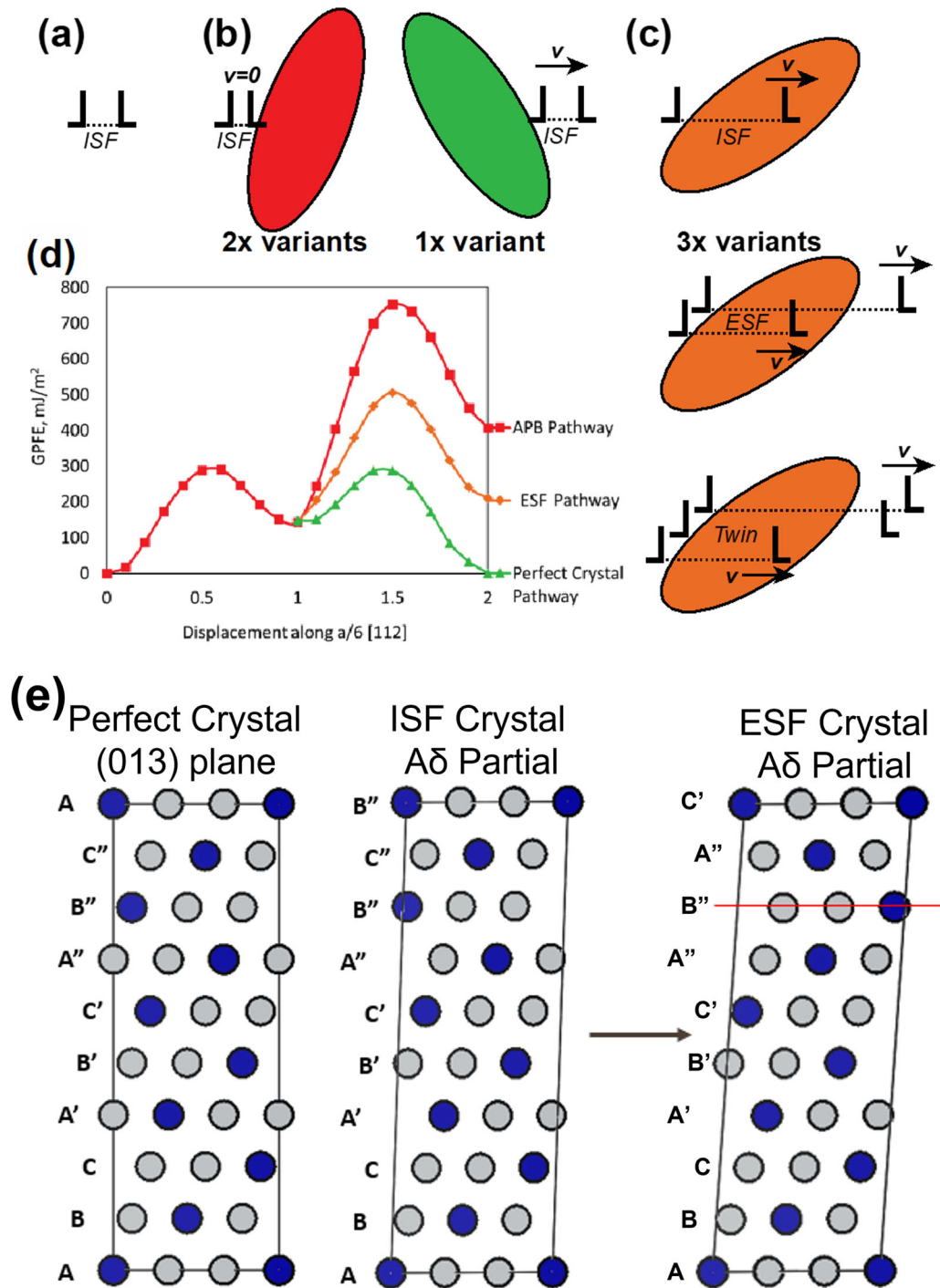


Fig. 13—Schematic showing interactions with (a) an $\frac{1}{2}\langle 110 \rangle$ -type matrix dislocation, where the dislocation will either (b) be blocked due to formation of a high energy CSF and APB energy (red pathway) or easily pass due to a small perfect translation of $\frac{1}{2}\langle 110 \rangle$ (green pathway), or (c) will form an ISF by passage of the leading $\frac{1}{2}\langle 211 \rangle$ type partial dislocation, followed by an ESF and eventually a microtwin after subsequent slip on adjacent planes. (d) DFT calculations of the slip pathway for each of the variants listed. (e) Atomistic schematic of pathway for ESF formation, as well as the DFT supercells used for calculations in (c) (Color figure online).

avoids strain localization and planar slip bands which reduces the damage accumulation that can be seen in γ' strengthened alloys. These deformation twins interacted with other twins and contributed to the work hardening as the twins must now proceed along the already twinned planes. Typically, deformation twinning is seen

as a detrimental aspect when it comes to fatigue life since fatigue crack propagation can extend along twin boundaries. However, other research^[32] has shown that HAYNES[®] 244[®] has good thermomechanical fatigue life. It is likely that deformation twinning at fatigue

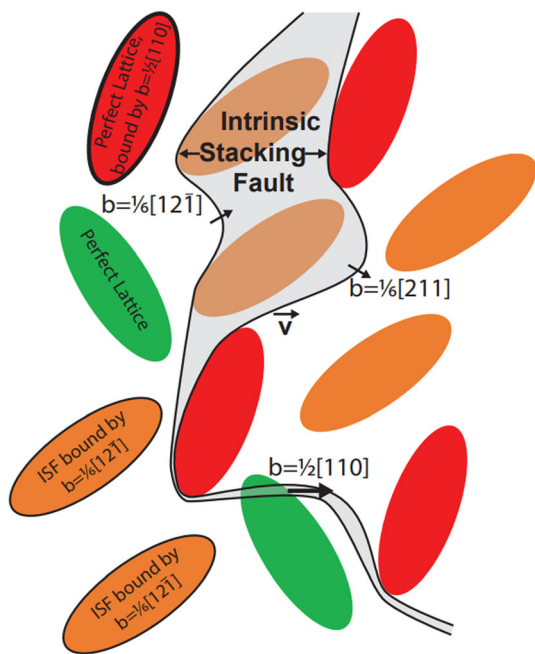


Fig. 14—Schematic showing how a single $\frac{1}{2}[110]$ matrix dislocation might shear through several variants on a given (111) plane. Red precipitates = formation of CSF upon passage of the leading $\frac{1}{6}[211]$ dislocation; orange precipitates = formation of ISF upon passage of the leading $\frac{1}{6}[211]$ dislocation; and green precipitates = full lattice translation by passage of a $\frac{1}{2}[110]$ dislocation (Color figure online).

crack tips can effectively blunt the tip and increase the fatigue life.

The addition of W to the 244 alloy improves the thermal stability of the precipitate, allowing an increase in the maximum operating temperature to 760 °C. The corresponding benefit in strength suggests that W is also increasing the fault energies of the precipitates. It is likely an increase in the stacking fault energy, γ_{sf} which controls the formation of the initial stacking fault that eventually thickens into a deformation twin. An increase in fault energy will require greater stress to form, thus improving the yield strength of the alloy over alloys that do not contain W. The higher temperature creep testing did show microstructural evolution occurring, indicating the γ''' phase is metastable at this elevated temperature, but still sufficiently stable to offer exceptional creep resistance. The microstructural evolution is a time, temperature, and stress-dependent reaction, which occurs significantly at 760 °C where variants that were unfavorably oriented to the applied stress dissolved, and precipitate variants that were well-oriented coarsened. The strain associated with the lenticular precipitates influences the stability of the precipitates as well as the growth kinetics.^[35] This phenomenon is still under investigation but does not significantly change the dominant deformation mechanisms in the samples investigated.

Microtwinning is observed in other Ni-base superalloys, but usually at high temperature and low stress, since the rate limiting process is a diffusion-controlled reordering around partial dislocations.^[38–41] However, the 244 alloy has deformation twinning seen at room temperature, as well as high temperature, likely limiting the influence of a diffusion-controlled process of local reordering. Nonetheless, this local reordering could be a possible mechanism at high temperature, especially in directions that an $\frac{1}{6}[112]$ partial dislocation would form a high energy complex stacking fault. This was not explicitly observed, but characterization of the formation of CSF over other stacking faults will require high resolution STEM imaging. However, as previously stated, the presence of variants that would form complex stacking faults does contribute to the strengthening aspect of the γ''' phase.

V. CONCLUSION

1. The dispersion of the coherent $\text{Ni}_2(\text{Cr, Mo, W})$ intermetallic phase significantly strengthens Haynes® 244® by restricting the motion of dislocations through the precipitates.
2. Planar slip is observed in mill annealed (precipitate-free) specimens during room temperature tensile testing.
3. Microtwin formation is observed in γ''' -containing specimens under tension and compression creep at temperatures and strain rates ranging from 27 °C to 760 °C and 10^{-4} to 10^{-9} s^{-1} , respectively.
4. Both intrinsic and extrinsic stacking faults are observed to form in the γ''' precipitates and adjacent γ matrix, and extended faults are observed to span multiple precipitates in 2 pct interrupted specimens.
5. Microtwins are observed to cut through other microtwins, and certain variants orientated in an unfavorable direction to the applied stress selectively dissolve in both untwinned and twinned regions, especially at elevated temperatures. This leaves variants oriented in favorable directions that coarsen.
6. High Antiphase Boundary and Complex Stacking Fault energies in the precipitate likely preclude shearing for half of the γ''' variants for a given $\frac{1}{2}[110]$ dislocation, instead facilitating deformation twinning through the other of the γ''' variants.

ACKNOWLEDGMENTS

This work was supported by a generous gift from Haynes International, Inc., the Purdue Electron Microscopy Facility, and through computational resources provided by Information Technology at

Purdue University, West Lafayette, Indiana. TM would like to thank Jennifer Schoolcraft and Victoria Tucker for their vital help in sample preparation and analysis.

CONFLICT OF INTEREST

The authors declare that they have no known competing financial interests or personal relationships that could have appeared to influence the work reported in this paper.

SUPPLEMENTARY INFORMATION

The online version contains supplementary material available at <https://doi.org/10.1007/s11661-022-06945-2>.

REFERENCES

1. T.M. Pollock and S. Tin: *J. Propuls. Power.*, 2006, vol. 22, pp. 361–74. <https://doi.org/10.2514/1.18239>.
2. E. Benini: *Advances in Gas Turbine Technology*, BoD - Books on Demand, Norderstedt, 2011.
3. R.C. Reed: *The Superalloys Fundamentals and Applications*, Cambridge University Press, Cambridge, 2006. <https://doi.org/10.1017/CBO9780511541285>.
4. R.E. Schafrik and R. Sprague: *Adv. Mater. Process.*, 2004, vol. 162, pp. 33–36.
5. R.C. Reed, T. Tao, and N. Warnken: *Acta Mater.*, 2009, vol. 57, pp. 5898–5913. <https://doi.org/10.1016/j.actamat.2009.08.018>.
6. J. Xie, S. Tian, X. Zhou, X. Yu, and W. Wang: *Mater. Sci. Eng. A*, 2012, vol. 538, pp. 306–14. <https://doi.org/10.1016/j.msea.2012.01.049>.
7. T.M. Smith, R.R. Unocic, H. Deutchman, and M.J. Mills: *Mater. High Temp.*, 2016, vol. 33, pp. 372–83. <https://doi.org/10.1080/09603409.2016.1180858>.
8. D.P. Pope: *Int. Met. Rev.*, 1984, <https://doi.org/10.1179/imtr.1984.29.1.136>.
9. L. Feng, D. Mcallister, C.H. Zenk, M.J. Mills, and Y. Wang, in *Superalloys 2020*, Springer, Cham, 2020, pp. 1055–65. <https://doi.org/10.1007/978-3-030-51834-9>.
10. O.I. Gorbato, I.L. Lomaev, Y.N. Gornostyrev, A. Ruban, D. Furrer, V. Venkatesh, D.L. Novikov, and S.F. Burlatsky: *Phys. Rev. B.*, 2016, vol. 93, pp. 1–8. <https://doi.org/10.1103/PhysRevB.93.224106>.
11. M. Dodaran, A.H. Etefagh, S.M. Guo, M.M. Khonsari, W.J. Meng, N. Shamsaei, and S. Shao: *Intermetallics (Barking)*, 2020, vol. 117, p. 106670. <https://doi.org/10.1016/j.intermet.2019.106670>.
12. N. Yang, Y. Wei, C. Song, and L. Jiao: *Jinshu Xuebao/Acta Metall. Sin.*, 1986, vol. 22, pp. 477–83.
13. M.S. Titus, Y.M. Eggeler, A. Suzuki, and T.M. Pollock: *Acta Mater.*, 2015, vol. 82, pp. 530–39. <https://doi.org/10.1016/j.actamat.2014.08.033>.
14. J.P. Hirth, J. Lothe, and T. Mura: *J. Appl. Mech.*, 1983, vol. 50, pp. 476–77. <https://doi.org/10.1115/1.3167075>.
15. B.H. Kear and H.G.F. Wilsdorf: *Trans. Am. Inst. Min. Metall. Pet. Eng.*, 1962, vol. 224, pp. 382–86.
16. L.E. Shilkrot, R.E. Miller, and W.A. Curtin: *J. Mech. Phys. Solids.*, 2004, <https://doi.org/10.1016/j.jmps.2003.09.023>.
17. G. Schoeck: *Philos. Mag. A*, 1999, vol. 79, pp. 1207–15. <https://doi.org/10.1080/01418619908210356>.
18. J. Wang and H. Sehitoglu: *Intermetallics (Barking)*, 2014, vol. 52, pp. 20–31. <https://doi.org/10.1016/j.intermet.2014.03.009>.
19. G. Molenat and D. Caillard: *Philos. Mag. A*, 1991, vol. 64, pp. 1291–1317. <https://doi.org/10.1080/01418619108225350>.
20. V. Vitek: *Intermetallics (Barking)*, 1998, vol. 6, pp. 579–85. [https://doi.org/10.1016/s0966-9795\(98\)00040-5](https://doi.org/10.1016/s0966-9795(98)00040-5).
21. M. Khantha, V. Vitek, and D.P. Pope: *Model. Simul. Mater. Sci. Eng.*, 1994, vol. 2, pp. 587–96. <https://doi.org/10.1088/0965-0393/2/3A/012>.
22. V.A. Vorontsov, C.M.F. Rae, C. Shen, Y. Wang, and D. Dye: *Acta Mater.*, 2010, vol. 58, pp. 4110–19. <https://doi.org/10.1016/j.actamat.2010.03.041>.
23. M. Yamaguchi, V. Paidar, D.P. Pope, and V. Vitek: *Philos. Mag. A*, 1982, vol. 45, pp. 867–82. <https://doi.org/10.1080/01418618208239909>.
24. F.D. León-Cázares, R. Schlütter, T. Jackson, E.I. Galindo-Nava, and C.M.F. Rae: *Acta Mater.*, 2020, vol. 182, pp. 47–59.
25. D.C. Lv, D. McAllister, M.J. Mills, and Y. Wang: *Acta Mater.*, 2016, vol. 118, pp. 350–61. <https://doi.org/10.1016/j.actamat.2016.07.055>.
26. T. Mann, M.G. Fahrman, and M.S. Titus: *Metall. Mater. Trans. A*, 2022, vol. 53A, pp. 4188–4206. <https://doi.org/10.1007/s11661-022-06797-w>.
27. M. Kumar and V.K. Vasudevan: *Acta Mater.*, 1997, vol. 45, pp. 3203–22. [https://doi.org/10.1016/S1359-6454\(97\)00007-4](https://doi.org/10.1016/S1359-6454(97)00007-4).
28. M. Kumar and V.K. Vasudevan: *Acta Mater.*, 1996, vol. 44, pp. 4865–80. [https://doi.org/10.1016/S1359-6454\(96\)00092-4](https://doi.org/10.1016/S1359-6454(96)00092-4).
29. X. Gao, R. Hu, T. Zhang, J. Li, L. Yuan, and J. Kong: *Mater. Charact.*, 2016, vol. 111, pp. 86–92. <https://doi.org/10.1016/j.matchar.2015.11.015>.
30. H.T. Vo, K. Dang, F. Teng, M. Schneider, B.P. Eftink, S.A. Maloy, J.D. Tucker, L. Capolungo, and P. Hosemann: *Mater. Des.*, 2021, <https://doi.org/10.1016/j.matdes.2021.109820>.
31. J.W. Christian and D.E. Laughlin: *Acta Metall.*, 1988, vol. 36, pp. 1617–42. [https://doi.org/10.1016/0001-6160\(88\)90230-1](https://doi.org/10.1016/0001-6160(88)90230-1).
32. M.G. Fahrman: *Proceedings of the ASME TurboExpo 2021 Conference, paper GT 2021-59619*.
33. M.G. Fahrman, S.K. Srivastava, and L.M. Pike: *MATEC Web of Conferences*, vol. 14, 2014. <https://doi.org/10.1051/mateconf/20141417004>.
34. N. Tsuno, S. Shimabayashi, K. Kakehi, C.M.F. Rae, and R.C. Reed: *Proceedings of the International Symposium on Superalloys*, 2008, pp. 433–42. https://doi.org/10.7449/2008/Superalloys_2008_433_442.
35. A. Verma, J.B. Singh, S.D. Kaushik, and V. Siruguri: *J. Alloys Compd.*, 2020, vol. 813, p. 152195. <https://doi.org/10.1016/j.jallcom.2019.152195>.
36. J. Song, R. Field, A. Clarke, Y. Fu, and M. Kaufman: *Acta Mater.*, 2019, vol. 165, pp. 362–72. <https://doi.org/10.1016/j.actamat.2018.11.063>.
37. J.W. Edington: *Practical Electron Microscopy in Materials Science*, Van Nostrand Reinhold Co., New York, 1976.
38. M. Sundararaman, P. Mukhopadhyay, and S. Banerjee: *Acta Metall.*, 1988, vol. 36, pp. 847–64. [https://doi.org/10.1016/0001-6160\(88\)90139-3](https://doi.org/10.1016/0001-6160(88)90139-3).
39. L.P. Freund, O.M.D.M. Messé, J.S. Barnard, M. Göken, S. Neumeier, and C.M.F. Rae: *Acta Mater.*, 2017, vol. 123, pp. 295–304. <https://doi.org/10.1016/j.actamat.2016.10.048>.
40. L. Kovarik, R.R. Unocic, J. Li, P. Sarosi, C. Shen, Y. Wang, and M.J. Mills: *Prog. Mater. Sci.*, 2009, vol. 54, pp. 839–73. <https://doi.org/10.1016/j.pmatsci.2009.03.010>.
41. M. Kolbe: *Mater. Sci. Eng. A*, 2001, vol. 319–21, pp. 383–87. [https://doi.org/10.1016/S0921-5093\(01\)00944-3](https://doi.org/10.1016/S0921-5093(01)00944-3).

Publisher's Note Springer Nature remains neutral with regard to jurisdictional claims in published maps and institutional affiliations.

Springer Nature or its licensor (e.g. a society or other partner) holds exclusive rights to this article under a publishing agreement with the author(s) or other rightsholder(s); author self-archiving of the accepted manuscript version of this article is solely governed by the terms of such publishing agreement and applicable law.